

# Non-Markovian Hole Excess Noise in Avalanche Amorphous Selenium Thin Films

Atreyo Mukherjee, Zhihang Han, Le Thanh Triet Ho, Abdul K. Rumaiz, Dragica Vasileska, and Amir H. Goldan\*



Cite This: *ACS Omega* 2023, 8, 23579–23586



Read Online

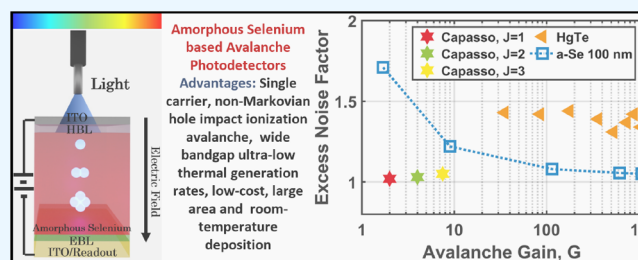
ACCESS |

Metrics & More

Article Recommendations

Supporting Information

**ABSTRACT:** Enhancing the signal-to-noise ratio in avalanche photodiodes by utilizing impact ionization gain requires materials exhibiting low excess noise factors. Amorphous selenium (*a*-Se) as a wide bandgap at  $\sim 2.1$  eV, a solid-state avalanche layer, demonstrates single-carrier hole impact ionization gain and manifests ultralow thermal generation rates. A comprehensive study of the history dependent and non-Markovian nature of hot hole transport in *a*-Se was modeled using a Monte Carlo (MC) random walk of single hole free flights, interrupted by instantaneous phonon, disorder, hole–dipole, and impact-ionization scattering interactions. The hole excess noise factors were simulated for 0.1–15  $\mu\text{m}$  *a*-Se thin-films as a function of mean avalanche gain. The hole excess noise factors in *a*-Se decreases with an increase in electric field, impact ionization gain, and device thickness. The history dependent nature of branching of holes is explained using a Gaussian avalanche threshold distance distribution and the dead space distance, which increases determinism in the stochastic impact ionization process. An ultralow non-Markovian excess noise factor of  $\sim 1$  was simulated for 100 nm *a*-Se thin films corresponding to avalanche gains of 1000. Future detector designs can utilize the nonlocal/non-Markovian nature of the hole avalanche in *a*-Se, to enable a true solid-state photomultiplier with noiseless gain.



## INTRODUCTION

Avalanche photodiodes (APDs) utilize the impact ionization phenomenon with enhanced signal-to-noise ratios (SNRs), to amplify weak signals above the noise floor of readout electronics with applications in photon counting and correlation studies, laser range finding, and medical imaging.<sup>1–6</sup> However, the APD gain contributes to its own shot noise component that grows proportionally with avalanche multiplication.<sup>7</sup> This omnipresent shot noise component of the measured noise current source ( $I_N$ ) can be expressed as  $I_{\text{ShotN}} = \sqrt{2qI_{\text{inj}}\langle G \rangle^2 \text{ENF}}$ , where  $q$  is an electronic charge,  $I_{\text{inj}}$  is the primary injected current into the avalanche junction,  $\langle G \rangle$  is the mean multiplication factor of the avalanche process, and ENF is the excess noise factor due to the stochastic nature of the impact ionization multiplication process. In a typical APD material, primary carriers (electron/hole) enter the high electric field region and gain sufficient kinetic energy greater than the material bandgap and collide with a lattice atom, thus breaking the lattice bond and generating secondary electron–hole pairs (the impact ionization process). These resulting pairs of secondary carriers are once again accelerated by the field and may further break more lattice bonds, resulting in tertiary carriers, and the avalanche *branching process* continues thereafter. Thus, the primary carrier rapidly multiplies by the successive impact ionization events until all the carriers exit the

high-field region.<sup>8,9</sup> In this impact ionization carrier *branching process*, the ENF is an additional source of noise originating as a result of the randomness in the positions at which secondary/tertiary carriers are generated (the positional randomness of avalanche gain),<sup>10</sup> and as a result of the feedback process associated with the fact that both electrons and holes can produce impact ionization events.<sup>8,11</sup> These two factors cumulatively result in variation of the total number of carriers produced per initial photocarrier (gain randomness), thus resulting in the noise source termed as the ENF.<sup>8,10</sup> Thus, for an arbitrary random avalanche multiplication gain variable  $G$  corresponding to every primary carrier, the ENF is calculated as follows:  $\text{ENF} = \langle G^2 \rangle / \langle G \rangle^2$ , where  $\langle G \rangle$  is the mean multiplication (first moment) and  $\langle G^2 \rangle$  is the mean of the squared multiplication (second moment).<sup>12,13</sup>

To enable SNR enhancement, an ideal APD material should exhibit small ENFs such that the detector noise is not dominated by its shot noise contribution. MacIntyre's local

Received: February 24, 2023

Accepted: May 4, 2023

Published: June 16, 2023



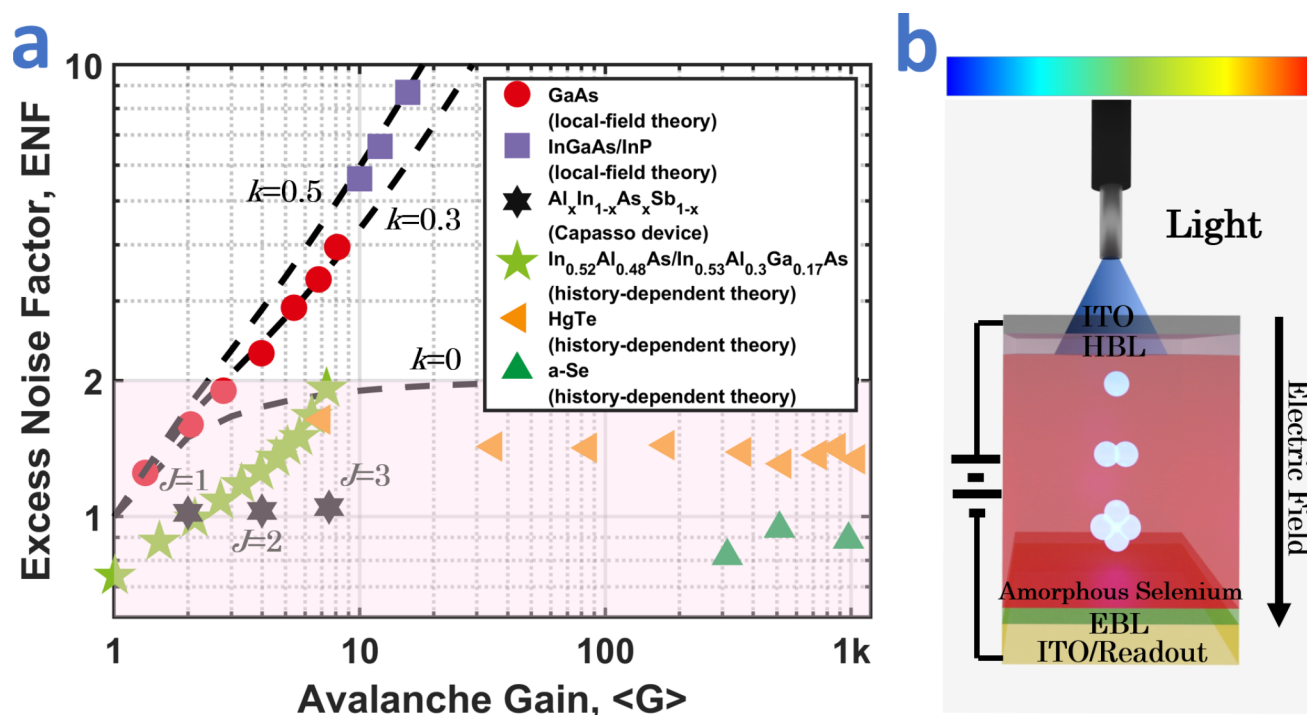


**Figure 1.** (a) ENF as a function of mean impact ionization avalanche gain compared for three different classes of APD materials. The dashed lines represent the McIntyre history independent model, which has been successfully explained by the local-field theory of impact ionization. Circle markers show measured ENF results for GaAs,<sup>14</sup> and square markers show measured ENF in InGaAs/InP APDs,<sup>15,16</sup> both matching the local-field theory McIntyre predictions corresponding to  $k \sim 0.3$  and  $k \sim 0.5$ , respectively. Hexagon markers show noiseless avalanche gains of up to about eight achieved in a Capasso device using adequately designed heterojunctions with maximum gain stages, with  $J = 3$  corresponding to a gain of eight.<sup>3</sup> Non-Markovian devices utilizing ultrathin submicron multiplicative regions are shown with pentagon<sup>20,21</sup> and left-pointing triangular markers.<sup>22</sup> Prior reports of ENF in a pickup-tube-based  $a$ -Se device are shown using upward-pointing triangular markers exhibiting an ENF of  $\sim 1$  at a gain  $\sim 1000$ .<sup>23</sup> (b) Schematic of a typical multilayer  $p$ - $i$ - $n$   $a$ -Se APD device as a viable alternative to the bulky, fragile, and field sensitive photomultiplier tube.<sup>5,24</sup> The  $a$ -Se layer can also be coupled to existing photon absorption layers, to be used as an efficient avalanche hole transport layer, thus covering applications ranging the entire visible electromagnetic spectrum.<sup>25</sup>

field theory states  $\text{ENF} = k\langle G \rangle + (1 - k)(2 - 1/\langle G \rangle)$ , where,  $k$  is the ratio of electron/hole to hole/electron impact ionization rate, as shown in Figure 1a. The McIntyre theory accurately predicts the ENF in crystalline APDs where carriers undergo ballistic impact ionization through a process called Markov (i.e., memoryless) branching, see Figure 1a. ENF measurements for two such devices are shown in Figure 1a utilizing GaAs<sup>14</sup> and InGaAs/InP based APDs,<sup>15,16</sup> which matches the McIntyre predictions corresponding to a  $k$  value of 0.3 and 0.5, respectively. The ENF limits the maximum useful gain of an APD, thus necessitating materials with small  $k$  values. For single carrier impact ionization,  $k \sim 0$ , the McIntyre prediction for ENF approaches a value of 2 for  $\langle G \rangle > 10$ . To achieve a more deterministic ionization behavior, the concept of band-structure engineering using semiconductor heterojunctions was proposed in the 1980s to ensure that only one carrier type undergoes impact ionization ( $k \sim 0$ ) specifically at the heterojunction band discontinuity where the probability of ionization spikes, thereby mimicking the behavior of a dynode in a vacuum photomultiplier tube.<sup>17</sup> Recently an ideal ENF of  $\sim 1$  has been observed in a staircase type Capasso device corresponding to a maximum number of cascaded asymmetric gain stages,  $J = 3/\langle G \rangle = 8$ ,<sup>3,18</sup> beyond which the ENF starts to deviate from the ideal Capasso model at  $G > 10$  due to fabrication challenges associated with the rigorous impact ionization engineering techniques required to yield  $k \sim 0$ .<sup>19</sup>

History dependence can be introduced in the carrier branching process in APDs, thus increasing determinism,

which further decreases the ENF below 2.<sup>9,16,26–28</sup> After an ionization event occurs, each carrier needs to travel a minimum distance, which is frequently referred to as the “dead space/length,” before it can gain sufficient energy from the electric field to have a nonnegligible ionization probability. When the thickness of the multiplication region becomes comparable to a “few” dead spaces/lengths, the nonlocal/non-Markovian history-dependent effects dominate.<sup>8</sup> This idea was utilized in non-Markovian devices with a measured  $\text{ENF} < 2$ , which exhibited an electron-only single-carrier avalanche, in two separate device structures, namely, crystalline compound InAlAs/InAlGaAs<sup>20,21</sup> and HgCdTe high-density, vertically integrated APDs.<sup>22,29</sup> Both devices utilized thin submicron multiplicative regions, which is an integer multiple of the “dead length/space”. These low ENF non-Markovian APD devices have resulted in significant progress in the field of infrared detection with improved gain-bandwidth products.<sup>30</sup> However, the non-Markovian devices until now have utilized small bandgap materials incompatible with room-temperature operation, resulting in higher leakage currents and rendering the avalanche process inimical to substantial SNR improvement.

Ultralow thermal generation rates<sup>31</sup> combined with a single carrier hole avalanche process renders  $a$ -Se to be either used as a short visible light absorbing APD responsive in the spectrum window of 400–450 nm where  $a$ -Se demonstrates an external quantum efficiency  $\sim 90\%$ <sup>5,32–36</sup> or coupled to existing photon absorbing layers just to be used as an efficient hole transport

layer (HTL) with avalanche capabilities, thus encompassing photonic applications across the visible electromagnetic spectrum, see Figure 1b.<sup>25</sup> Moreover, it can be uniformly deposited near room-temperature over larger areas as compared to crystalline semiconductors and is compatible with readout electronics.<sup>37,38</sup> At high electric fields, hole transport in *a*-Se can be shifted entirely from localized to extended states, resulting in a single carrier hole impact ionization avalanche with prior reports of ENF  $\sim 1$ , corresponding to a gain of  $\sim 1000$ , as shown in Figure 1a,<sup>23</sup> indicating the existence of a peculiar noise reduction mechanism in the hole avalanche process in *a*-Se. Thus, modeling the extended states transport of “hot” holes involved in the single carrier impact ionization phenomenon is pivotal to the understanding of the nature of avalanche gain and excess noise in *a*-Se-based detectors.<sup>39–42</sup>

## RESULTS AND DISCUSSION

The first theories to study impact ionization date back to the 1930s. Shockley proposed the lucky-electron model, which described impact ionization as a process initiated by ballistic carriers that do not undergo collision. A major problem with the Shockley model is the absence of sufficient ballistic electrons to validate experimentally measured gain. The lucky-drift model proposed by Ridley was based on the assumption that momentum relaxation rate is much faster than the energy relaxation rate.<sup>43</sup> Here, the impact ionization occurs predominantly either by lucky-ballistic motion or lucky-drift (carriers drift in an electric field with momentum-relaxing collisions without there being in the same period any significant energy relaxation) or a combination of both. Kasap and Rubel implemented a modified lucky-drift model for *a*-Se.<sup>44,45</sup> A feature of the modified lucky-drift model is an explicit treatment of elastic scattering due to the disorder potential inherent to amorphous solids, in addition to the inelastic scattering by nonpolar optical and acoustic phonons. The scattering by a disorder potential is assumed to be the dominant mechanism of the momentum relaxation for energetic electrons.<sup>46–49</sup> In this work, we use an MC-based multiscale simulation framework, see Supporting Information (SI) section S1, to calculate the ENF as a function of gain and thickness in bulk *a*-Se films. Our work for the first time laid down quantum mechanical formulations using Fermi’s golden rule to calculate energy dependent phonon scattering (acoustic, polar optical emission/absorption, and nonpolar optical emission/absorption), hole-dipole scattering (caused by valence alternate pair type defects as scattering centers), disorder scattering (to account for the lack of long-range order in the amorphous phase), and impact ionization scattering rates in *a*-Se, as shown in Figure 2a.<sup>39,50</sup> The energy and momentum relaxation dynamics of the individual scattering mechanisms are summarized in Table 1. The predictive capabilities of the MC based multiscale simulation framework for *a*-Se has been previously validated with experimental findings of time-of-flight mobility, ensemble energy and drift velocity, and field dependent hole impact ionization gain and coefficients.<sup>39,40,50</sup>

The ENF calculations in the MC simulation framework proceeds with a single hole being introduced into the high electric field region with a randomly distributed kinetic energy around the mean of  $3/2k_B T$ , where  $k_B$  is the Boltzmann constant and  $T$  is the temperature. The corresponding wavevectors are calculated using a nonparabolic  $E-k$  relation

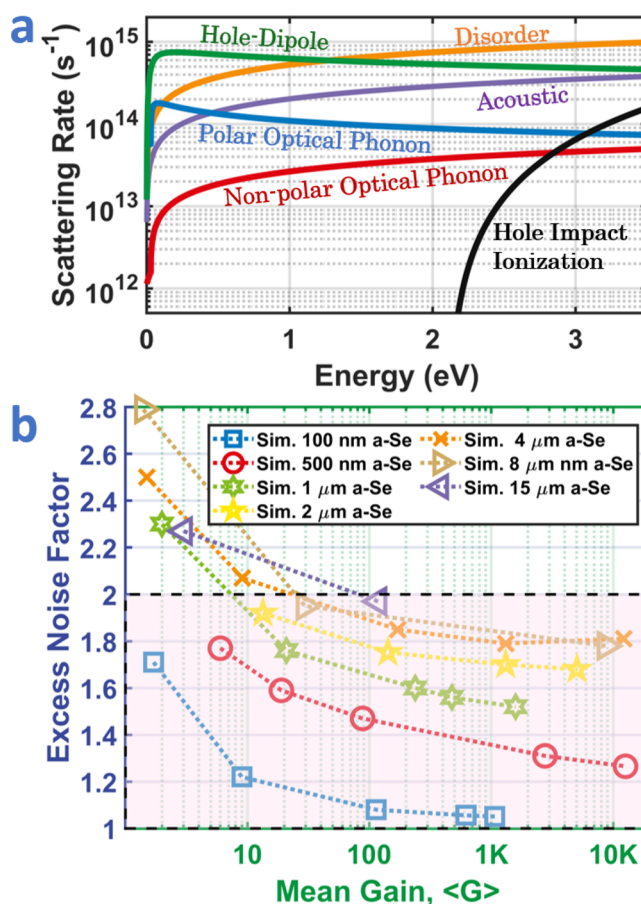


**Figure 2.** (a) Relevant hole scattering mechanisms in *a*-Se as a function of hole energies up to 3.5 eV. The complete derivations for each of the scattering mechanisms are provided in our previous work.<sup>50</sup> Although polar and nonpolar optical phonon absorption and emission processes are treated as separate scattering mechanisms, we show a cumulative sum of the absorption and emission processes. Figure reproduced with permission from ref 50. Copyright 2021 American Chemical Society. (b) Plot of ENF from single hole MC-BTE simulations for 0.1–15 μm *a*-Se bulk drift lengths as a function of mean gain,  $\langle G \rangle$ .

**Table 1. Energy and Momentum Relaxation Dynamics of the Scattering Mechanisms in *a*-Se**

mechanism	energy relaxation	momentum relaxation
acoustic phonon	elastic	isotropic
nonpolar optical phonon	inelastic	isotropic
polar optical phonon	inelastic	anisotropic
disorder	elastic	isotropic
hole-dipole	elastic	anisotropic
hole impact ionization	inelastic	isotropic

with a nonparabolicity factor of 0.15.<sup>39,50</sup> As the hole is accelerated, phonon, hole–dipole, and disorder scattering delay its attainment of the ionization energy. The calculation of ENF in the hole branching process follows with the restrictions that there is no hole–hole interaction in the bulk region except at the moment of impact ionization. The hole initiated impact ionization process in *a*-Se involves a “hot” hole in the valence band that ionizes an electron residing in the valence band across the bandgap into the conduction band, leading to an extra positive charge in the valence band and a negative charge in the conduction band. This has been modeled using a single

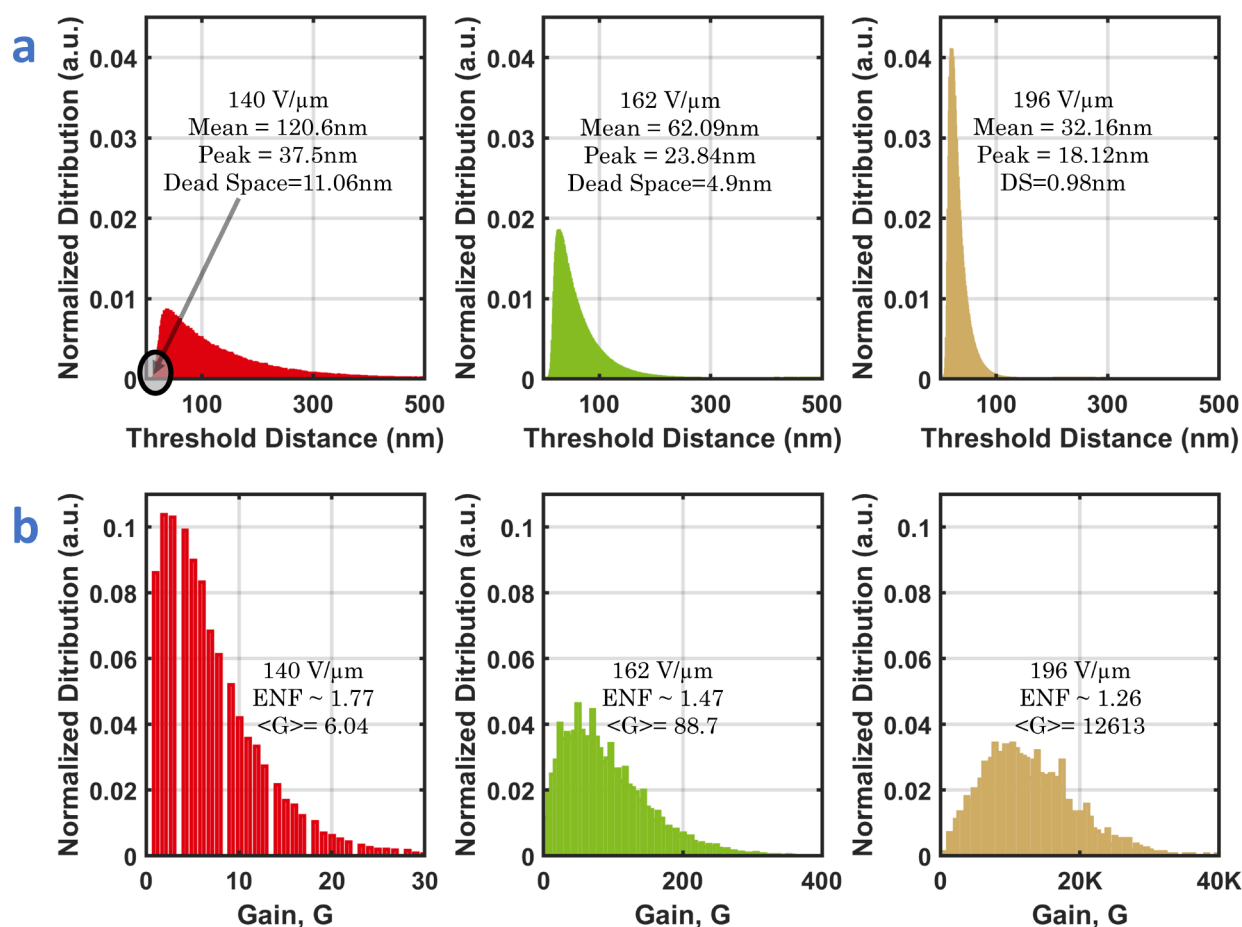


**Figure 3.** (a) Threshold distance distributions and (b) avalanche gain distribution for 500 nm *a*-Se bulk drift lengths for electric field strengths of 140, 162, and 196 V/μm, respectively.

term power law fit with a soft ionization threshold energy approximately equal to the band gap of *a*-Se  $\approx 2.1$  eV.<sup>40</sup> When the soft ionization threshold energy is crossed and the impact ionization scattering interaction is selected from a normalized cumulative scattering table, the holes position projected onto the field axis is recorded. The energy remaining for the two new holes (after the ionization energy is subtracted) is randomly partitioned and the trajectory for the hole carrier resumes with a randomized velocity corresponding to its share of the energy. The primary and secondary hole carriers resume to be accelerated by the electric field and interrupted by instantaneous scattering interactions until once again the impact ionization threshold energy is crossed and the impact ionization scattering interaction is selected. The avalanche process continues in this process until the primary and subsequently generated holes are collected at the end of the simulated drift length. At least 10 000 single hole MC trajectories were run in this fashion, and the avalanche gain from each of these single-hole MC trajectories was recorded to calculate the ENF for a certain thickness of *a*-Se and at an applied electric field. The ENF is calculated using the following:  $ENF = \langle G^2 \rangle / \langle G \rangle^2$ , where  $G$  is the gain from every single hole MC run, for a fixed electric field strength and a fixed *a*-Se drift length. The calculated ENF as a function of mean gain,  $\langle G \rangle$ , is shown in Figure 2b for simulated *a*-Se drift lengths from 0.1 to 15 μm. From Figure 2b, we see that the ENF decreases with an increase in avalanche gain and hence electric field. From Figure 2b, our simulation shows that the

non-Markovian nature of hot hole branching dominates for thinner layers of *a*-Se, resulting in smaller simulated ENFs under the initial assumption of single carrier impact ionization. For 100 nm *a*-Se films, the ENF is estimated to be  $\sim 1$ , at a gain value of 1000.

In each of the single hole MC simulations, each time a carrier underwent impact ionization, the distance between a hole's birth and its attainment of impact ionization energy was scored in a histogram. Figure 3a shows this threshold distance distribution for a 500 nm *a*-Se thin-film, for increasing strengths of the simulated electric field. Once again, we show the gain distribution results for a 500 nm simulated *a*-Se drift length in Figure 3b to demonstrate the nonlocal/non-Markovian nature of "hot" hole branching, with increasing electric fields. The complete detailed plots of threshold distance and avalanche gain distributions for *a*-Se bulk thicknesses ranging from 0.1 to 15 μm at various electric fields, are shown in the SI section S1.1.

In Figure 3a, no impact ionization occurs within the "dead space" (DS) distance, termed as the minimum threshold distance distribution. For thick *a*-Se bulk layers, the DS can be neglected, see SI section 1.1 and Figure S8. However, for thinner *a*-Se bulk layers, the nonlocal and non-Markovian nature of the impact ionization avalanche dominates when primary and secondary carriers initially enter the multiplication region and traversing a certain distance is required to attain sufficient energy to ionize. Moreover, the final states after ionization are typically near the band edge where the carrier

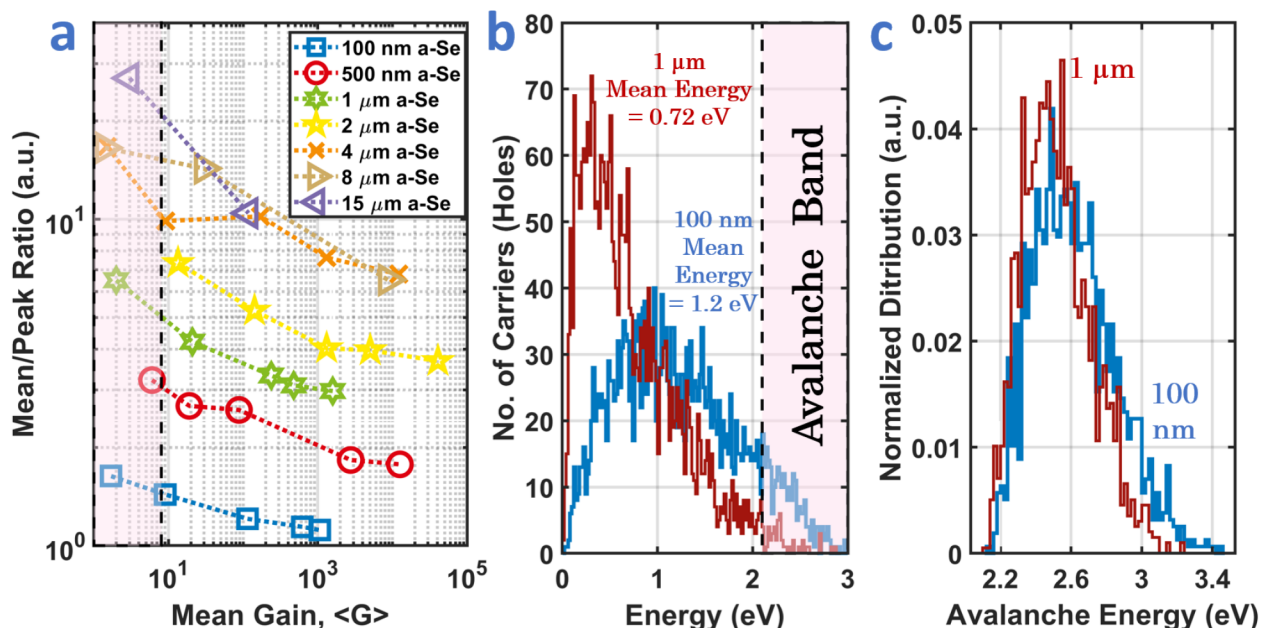


**Figure 4.** (a) The ratio of the mean to the peak of the threshold distance distribution, varying as a function of gain for 0.1–15  $\mu\text{m}$  *a*-Se bulk drift lengths. The red patch shows that, as the bulk *a*-Se length decreases, the mean/peak ratios decrease at smaller values of  $\langle G \rangle$  (1–10) across 0.1–15  $\mu\text{m}$  *a*-Se thicknesses. (b) Hole energy distributions for 1  $\mu\text{m}$  and 100 nm *a*-Se simulated drift lengths, respectively. Beyond the onset of impact ionization, thinner simulated drift lengths have a Gaussian hole energy distribution. (c) The distribution of hole energies at which the impact ionization scattering mechanism is selected, in 1  $\mu\text{m}$  and 100 nm *a*-Se simulated drift lengths, respectively.

energy is orders of magnitude less than the ionization threshold  $\sim 2.1$  eV. The threshold distance distribution as shown in Figure 3a has a mean of 120 nm, which is about 24% of the entire avalanche region in the 500 nm *a*-Se layer at 140 V/ $\mu\text{m}$ . The shift from an exponential threshold distance distribution in Figure 3a at 140 V/ $\mu\text{m}$ , to a Gaussian distribution at 196 V/ $\mu\text{m}$ , is replicated in the change in shape of the gain distributions, further resulting in a decrease in ENF with an increase in electric field, as shown in Figure 3b.

As the applied electric field and hence the mean hole energy in the *a*-Se layer increases, polar optical phonon and hole–dipole scattering interactions have a diminished influence, as shown in Figure 3a, where the DS decreases from  $\sim 11$  nm to less than 1 nm as the electric field increases from 140 V/ $\mu\text{m}$  to 196 V/ $\mu\text{m}$ , respectively. This suggests that the DS plays a diminished role in the decrease in ENF with an increase in electric field. However, as the electric field increases, the tail of the threshold distance distribution decreases. Since the width of the threshold distance distribution decreases significantly faster than the contraction in the dead space, the net result is that the ionization process becomes more deterministic with an increase in electric field.<sup>8</sup> This idea is demonstrated in Figure 4a, where with an increase in avalanche gain and hence electric field, the initial mean/peak ratio as shown by the red patch decreases. When the peak and the mean of the threshold distance distribution coincide, as in 100 nm *a*-Se simulated drift lengths, see SI section S1.1, Figure S2, the perfectly non-Markovian ENF of  $\sim 1.05$  is simulated corresponding to a gain of 1000. Plots of the mean and the peak of the threshold distance distribution changing as a function of simulated drift length and avalanche gain is provided in SI section S1.2 and Figure S9. Thereafter, we simulated the hole energy distributions for two thicknesses of *a*-Se at an electric field beyond the onset of impact ionization. In Figure 4b, we show the hole energy distributions for 1000 holes simulated for an *a*-

Se drift length of 1  $\mu\text{m}$  and 100 nm, at an electric field of 120 V/ $\mu\text{m}$  and 170 V/ $\mu\text{m}$ , respectively. The shaded region marks the allowable impact ionization energy band (the energy tail of 2.1 eV and beyond where holes undergo an impact ionization avalanche). At 170 V/ $\mu\text{m}$  and for a 100 nm *a*-Se drift length, the total number of carriers at the end of the simulation was 2575, while at 120 V/ $\mu\text{m}$  and for 1  $\mu\text{m}$  *a*-Se drift length, the total number of carriers at the end of the simulation was 2979. From Figure 4b, we can see that, as the thickness of the *a*-Se layer decreases, the mean energy of the holes increases. Beyond the onset of impact ionization, thinner 100 nm *a*-Se layers demonstrate a more Gaussian energy distribution where the mean energy of the carriers is 1.2 eV, almost half of the soft impact ionization threshold energy of  $\sim 2.1$  eV. In Figure 4b, each time a hole impact ionization scattering interaction was selected, the energy of the hole at the point of impact ionization was tabulated, and the normalized distribution for the avalanche energy range is shown in Figure 4c for 100 nm and 1  $\mu\text{m}$  *a*-Se simulated drift lengths, respectively. We observe that irrespective of the simulated drift length, the avalanche energy range shows an almost similar narrow normal distribution with the distribution shifting slightly to higher energies for 100 nm *a*-Se thin films.

Next, to unequivocally show the positive effects of increasing gain and electric field on the internal averaging of ENF, we run 1000 single hole MC trajectories from birth to impact ionization. In Figure 5, we show five randomly selected hole trajectories, where the energy of the hole accelerated toward the direction of the electric field and interrupted by instantaneous scattering events within the framework of the MC algorithm is tabulated at every simulation step. The shaded region marks the lower soft threshold energy for impact ionization. From Figure 5a, we observe that at 120 V/ $\mu\text{m}$  the time taken for the randomly selected holes varies significantly by more than 2 orders of magnitude. The inset in Figure 5a

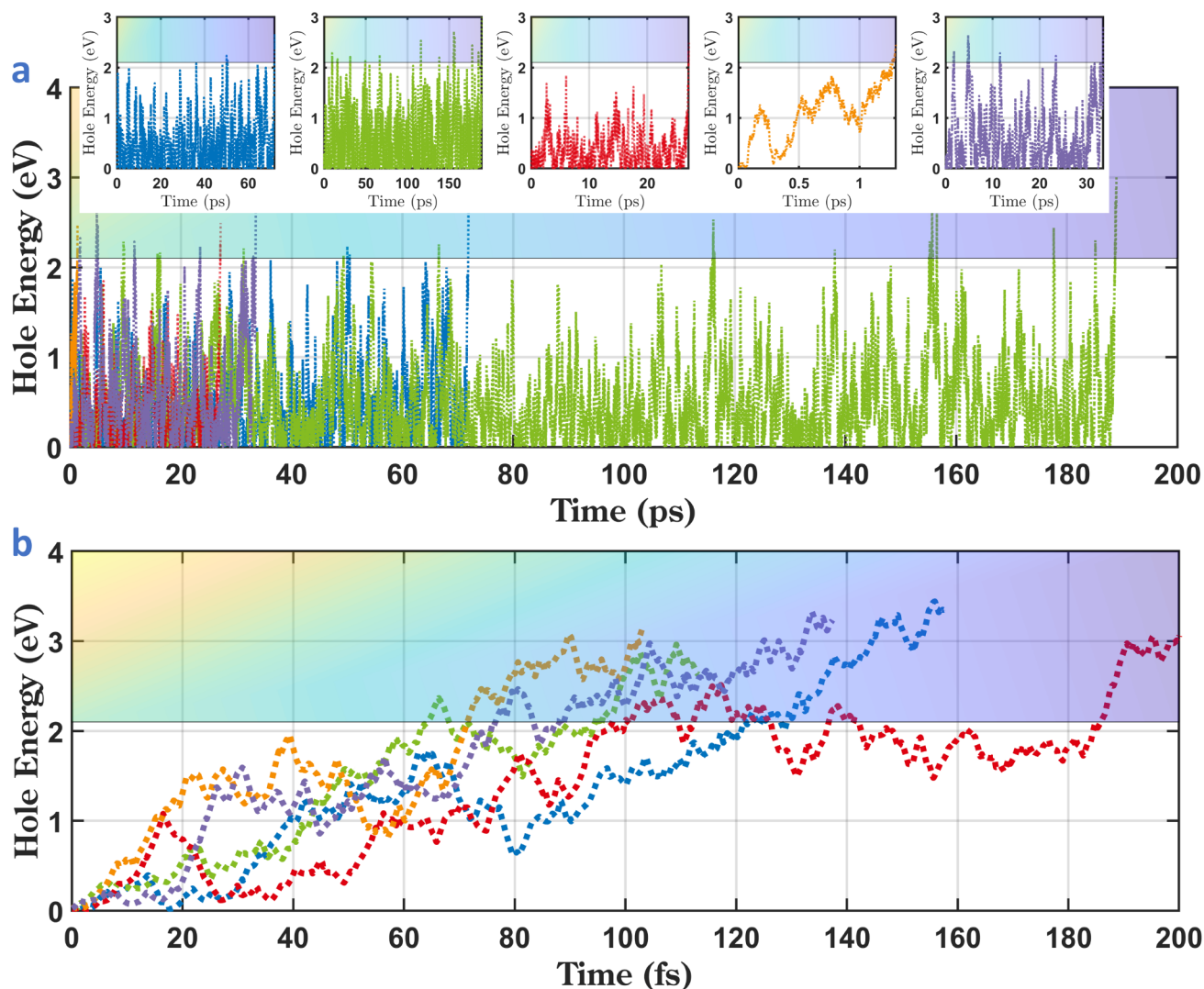


**Figure 5.** Plot of single MC simulations showing energy as a function of simulation drift time at (a)  $120 \text{ V}/\mu\text{m}$  and (b)  $380 \text{ V}/\mu\text{m}$  for five holes randomly selected from 1000 hole trajectories tracked until the first impact ionization event. The deterministic nature and internal averaging of avalanche gain in *a*-Se dominates as the electric field is increased from  $120 \text{ V}/\mu\text{m}$  in (a) to  $380 \text{ V}/\mu\text{m}$  in (b). The shaded regions show the allowable ionization energy range beyond the soft impact ionization threshold of 2.1 eV in the MC simulation framework.

shows the individual trajectories of the five randomly selected carriers. We can observe that crossing the impact ionization threshold does not ensure ionization. Energy loss phonon and disorder scattering mechanisms lead to the carrier energies decreasing below the soft ionization threshold, before a favorable impact ionization scattering interaction is selected. However, with an increase in electric field, see Figure 5b, the holes have a deterministic rise in energy to impact ionization; i.e., the rise to impact ionization for individual carriers have become synchronous in time. At high electric fields, as polar-optical phonon and hole-dipole scattering mechanisms becomes less significant, the hole carriers acquire near-ballistic velocities, and ionize quickly after achieving the impact ionization threshold energy. Thus, an increase in avalanche gain due to increasing electric field in *a*-Se, results in an internal averaging of the noise due to the stochastic avalanche process.

## CONCLUSION

In summary, the performance of APDs in terms of SNR and operating bandwidth is limited due to the noise associated with

the random nature of impact ionization.<sup>8</sup> This additional stochastic impact ionization ENF in APDs occurs due to the randomness in the locations at which ionizations may occur and the feedback process associated with the fact that both kinds of carrier can produce impact ionization. *a*-Se is the only wide band gap ( $\sim 2.1 \text{ eV}$ ) noncrystalline semiconductor that produces reliable and repeatable single carrier (holes) avalanche gain, without breakdown. In this work, a comprehensive study of the microscopic and macroscopic details of the hole impact ionization process in disordered *a*-Se was presented. The transport of holes in *a*-Se was simulated by using an in-house MC technique in which the carrier free-flights are interrupted by scattering from acoustic, polar, and nonpolar optical phonons, disorder, dipole, and impact ionization scattering interactions. The single carrier hole ENF in *a*-Se assuming electric field independent hole/electron  $k \sim 0$  was simulated as a function of layer thickness and applied electric field for  $0.1\text{--}15 \mu\text{m}$  thin films. The hole ENF in *a*-Se decreases with an increase in electric field, impact ionization gain and *a*-Se layer thickness, due to the existence of a nonzero dead space, and the nonballistic nature of hole

transport in *a*-Se, fostered by frequent scattering at high electric fields. This trend is substantiated more as the bulk layer thickness decreases. The history dependent nature of branching of *Hot* holes is explained using a Gaussian threshold distance distribution and the *dead space* distance which increases determinism in the stochastic impact ionization process. With increasing electric fields, the width of the threshold distance distribution tapers faster than the contraction in the dead space, and consequently the ionization process becomes more deterministic. Furthermore, with increasing electric fields, polar-optical phonon and hole-dipole scattering become less significant, as the carriers acquire near-ballistic velocities, and the time taken for impact ionization for individual holes becomes comparable and synchronous in time. An almost ideal non-Markovian hole ENF of  $\sim 1$  was simulated in the case of 100 nm *a*-Se thin films and avalanche gains of 1000. Hence, future detector designs can utilize the nonlocal/non-Markovian nature of the hole avalanche in *a*-Se, to enable a true solid-state photomultiplier with noiseless gain and enhanced SNRs.

## ■ ASSOCIATED CONTENT

### SI Supporting Information

The Supporting Information is available free of charge at <https://pubs.acs.org/doi/10.1021/acsomega.3c01256>.

Further details on the multiscale Monte Carlo Boltzmann transport equation solver simulation framework and details on calculating the threshold distance and gain distribution, as well as additional plots for the threshold and gain distributions in 0.1–15  $\mu\text{m}$  *a*-Se thin films (PDF)

## ■ AUTHOR INFORMATION

### Corresponding Author

Amir H. Goldan – Department of Radiology, Weill Cornell Medical College, Cornell University, New York, New York 10021, United States; Phone: +1-212-746-6000; Email: [amg4017@med.cornell.edu](mailto:amg4017@med.cornell.edu)

### Authors

Atreyo Mukherjee – Department of Electrical Engineering, College of Engineering and Applied Sciences, Stony Brook University, Stony Brook, New York 11794, United States; [orcid.org/0000-0002-8451-7167](https://orcid.org/0000-0002-8451-7167)

Zhihang Han – Department of Electrical Engineering, College of Engineering and Applied Sciences, Stony Brook University, Stony Brook, New York 11794, United States

Le Thanh Triet Ho – Department of Electrical Engineering, College of Engineering and Applied Sciences, Stony Brook University, Stony Brook, New York 11794, United States; [orcid.org/0000-0003-4984-467X](https://orcid.org/0000-0003-4984-467X)

Abdul K. Rumaiz – National Synchrotron Light Source II, Brookhaven National Laboratory, Upton, New York 11973, United States

Dragica Vasileska – School of Electrical, Computer, and Energy Engineering, Arizona State University, Tempe, Arizona 85287, United States

Complete contact information is available at:

<https://pubs.acs.org/doi/10.1021/acsomega.3c01256>

### Notes

The authors declare no competing financial interest.

## ■ ACKNOWLEDGMENTS

A.H.G. acknowledges the financial support from the National Science Foundation (ECCS 2323398). D.V. acknowledges the financial support from the National Science Foundation (ECCS 2025490 and ECCS 2048400). The authors acknowledge Research Computing at Arizona State University for providing (HPC, storage, etc.) resources that have contributed to the research results reported in this paper.

## ■ REFERENCES

- (1) Son, B.; Wang, Y.; Luo, M.; Lu, K.; Kim, Y.; Joo, H.-J.; Yi, Y.; Wang, C.; Wang, Q. J.; Chae, S. H.; Nam, D. Efficient Avalanche Photodiodes with a WSe<sub>2</sub>/MoS<sub>2</sub> Heterostructure via Two-Photon Absorption. *Nano Lett.* **2022**, *22*, 9516.
- (2) Paraiso, T. K.; Roger, T.; Marangon, D. G.; De Marco, I.; Sanzaro, M.; Woodward, R. I.; Dynes, J. F.; Yuan, Z.; Shields, A. J. A photonic integrated quantum secure communication system. *Nat. Photon* **2021**, *15*, 850–856.
- (3) March, S. D.; Jones, A. H.; Campbell, J. C.; Bank, S. R. Multistep staircase avalanche photodiodes with extremely low noise and deterministic amplification. *Nat. Photon* **2021**, *15*, 468–474.
- (4) LaBella, A.; Stavro, J.; Léveillé, S.; Zhao, W.; Goldan, A. H. Picosecond time resolution with avalanche amorphous selenium. *ACS Photon* **2019**, *6*, 1338–1344.
- (5) Kannan, H.; Stavro, J.; Mukherjee, A.; Léveillé, S.; Kisslinger, K.; Guan, L.; Zhao, W.; Sahu, A.; Goldan, A. H. Ultralow dark currents in avalanche amorphous selenium photodetectors using solution-processed quantum dot blocking layer. *ACS Photon* **2020**, *7*, 1367–1374.
- (6) Kannan, H.; Stavro, J.; Mukherjee, A.; Zhao, W.; Goldan, A.; Sahu, A. Colloidal Quantum Dots for Enhancing Performance of Avalanche Amorphous-Selenium Photodetectors. *Electrochemical Society Meeting Abstracts* **2021**, *239*, 911–911.
- (7) Bianconi, S.; Lauhon, L. J.; Mohseni, H. Exaggerated sensitivity in photodetectors with internal gain. *Nature Photon* **2021**, *15*, 714–714.
- (8) Campbell, J. C. Evolution of low-noise avalanche photodetectors. *IEEE J. Sel. Top. Quantum.* **2022**, *28*, 1.
- (9) LaViolette, R. A.; Stapelbroek, M. A non-Markovian model of avalanche gain statistics for a solid-state photomultiplier. *J. Appl. Phys.* **1989**, *65*, 830–836.
- (10) Saleh, B. E.; Hayat, M. M.; Teich, M. C. Effect of dead space on the excess noise factor and time response of avalanche photodiodes. *IEEE transactions on electron devices* **1990**, *37*, 1976–1984.
- (11) Saleh, B.; Teich, M.; Slusher, R. E. *Fundamentals of Photonics*; John Wiley & Sons, Inc., 1992; Vol. 45; pp 87–88.
- (12) Marsland, J.; Woods, R.; Brownhill, C. Lucky drift estimation of excess noise factor for conventional avalanche photodiodes including the dead space effect. *IEEE transactions on electron devices* **1992**, *39*, 1129–1135.
- (13) Hakim, N.; Saleh, B.; Teich, M. Generalized excess noise factor for avalanche photodiodes of arbitrary structure. *IEEE transactions on electron devices* **1990**, *37*, 599–610.
- (14) Ong, D.; Li, K.; Rees, G.; Dunn, G.; David, J.; Robson, P. A Monte Carlo investigation of multiplication noise in thin p<sup>+</sup>-i-n<sup>+</sup> GaAs avalanche photodiodes. *IEEE Trans. Electron Devices* **1998**, *45*, 1804–1810.
- (15) Yuan, P.; Hansing, C.; Anselm, K.; Lenox, C.; Nie, H.; Holmes, A.; Streetman, B.; Campbell, J. Impact ionization characteristics of III-V semiconductors for a wide range of multiplication region thicknesses. *IEEE J. Quantum Electron.* **2000**, *36*, 198–204.
- (16) Lee, S.; Jin, X.; Jung, H.; Lewis, H.; Liu, Y.; Guo, B.; Kodati, S. H.; Schwartz, M.; Grein, C.; Ronningen, T.; David, J. P. R.; Campbell, J. C.; Krishna, S. High gain, low noise 1550 nm GaAsSb/AlGaAsSb avalanche photodiodes. *Optica* **2023**, *10*, 147–154.
- (17) Capasso, F.; Tsang, W.-T.; Williams, G. F. Staircase solid-state photomultipliers and avalanche photodiodes with enhanced ionization rates ratio. *IEEE Trans. Electron Devices* **1983**, *30*, 381–390.

- (18) David, J. Photodetectors: The staircase photodiode. *Nat. Photonics* **2016**, *10*, 364–366.
- (19) Williams, G. M.; Compton, M.; Ramirez, D. A.; Hayat, M. M.; Huntington, A. S. Multi-Gain-Stage InGaAs Avalanche Photodiode With Enhanced Gain and Reduced Excess Noise. *IEEE J. Electron. Devices Soc.* **2013**, *1*, 54–65.
- (20) Campbell, J. C. Recent advances in avalanche photodiodes. *J. Light. Technol.* **2016**, *34*, 278–285.
- (21) Duan, N.; Wang, S.; Ma, F.; Li, N.; Campbell, J. C.; Wang, C.; Coldren, L. A. High-speed and low-noise SACM avalanche photodiodes with an impact-ionization-engineered multiplication region. *IEEE Photon. Technol. Lett.* **2005**, *17*, 1719–1721.
- (22) Rogalski, A. In *Mid-infrared Optoelectronics*; Tournié, E., Cerutti, L. Woodhead Publishing Series in Electronic and Optical Materials; Woodhead Publishing, 2020; pp 235–335.
- (23) Tsuji, K.; Takasaki, Y.; Hirai, T.; Yamazaki, J.; Tanioka, K. Avalanche phenomenon in amorphous selenium. *Optoelectron. Devices Technol.* **1994**, *9*, 367–378.
- (24) Scheuermann, J. R.; Howansky, A.; Hansroul, M.; Léveillé, S.; Tanioka, K.; Zhao, W. Toward scintillator high-gain avalanche rushing photoconductor active matrix flat panel imager (SHARP-AMFPI): initial fabrication and characterization. *Med. Phys.* **2018**, *45*, 794–802.
- (25) Mukherjee, A.; Kannan, H.; Triet Ho, L. T.; Han, Z.; Stavro, J.; Howansky, A.; Nooman, N.; Kisslinger, K.; Léveillé, S.; Kizilkaya, O.; et al. Vertical Architecture Solution-Processed Quantum Dot Photodetectors with Amorphous Selenium Hole Transport Layer. *ACS Photon* **2023**, *10*, 134–146.
- (26) Pilotto, A.; Esseni, D.; Selmi, L.; Palestri, P. Accurate Nonlocal Impact Ionization Models for Conventional and Staircase Avalanche Photodiodes Derived by Full Band Monte Carlo Transport Simulations. *IEEE J. Quantum Electron.* **2022**, *58*, 1–11.
- (27) Yi, X.; Xie, S.; Liang, B.; Lim, L. W.; Cheong, J. S.; Debnath, M. C.; Huffaker, D. L.; Tan, C. H.; David, J. P. Extremely low excess noise and high sensitivity  $\text{AlAs}_{0.56}\text{Sb}_{0.44}$  avalanche photodiodes. *Nature Photon* **2019**, *13*, 683–686.
- (28) Ramirez, D. A.; Hayat, M. M.; Huntington, A. S.; Williams, G. M. Non-local model for the spatial distribution of impact ionization events in avalanche photodiodes. *IEEE Photon. Technol. Lett.* **2014**, *26*, 25–28.
- (29) Kinch, M.; Beck, J.; Wan, C.-F.; Ma, F.; Campbell, J. HgCdTe electron avalanche photodiodes. *J. Electron. Mater.* **2004**, *33*, 630–639.
- (30) Chee, K.-W. II–VI Compound Semiconductor Avalanche Photodiodes for the Infrared Spectral Region: Opportunities and Challenges. *Handbook of II-VI Semiconductor-Based Sensors and Radiation Detectors*; Springer: Cham, 2023; Vol. 2: Photodetectors; pp 53–77.
- (31) Ho, L. T. T.; Mukherjee, A.; Vasileska, D.; Akis, J.; Stavro, J.; Zhao, W.; Goldan, A. H. Modeling Dark Current Conduction Mechanisms and Mitigation Techniques in Vertically Stacked Amorphous Selenium-Based Photodetectors. *ACS Appl. Electron. Mater.* **2021**, *3*, 3538–3546.
- (32) Huang, H.; Abbaszadeh, S. Recent developments of amorphous selenium-based X-ray detectors: a review. *IEEE Sens. J.* **2020**, *20*, 1694–1704.
- (33) Arnab, S. M.; Kabir, M. A novel amorphous selenium avalanche detector structure for low dose medical X-ray imaging. *IEEE Trans. Radiat. Plasma Med. Sci.* **2020**, *4*, 319–326.
- (34) Scheuermann, J. R.; Goldan, A. H.; Tousignant, O.; Léveillé, S.; Zhao, W. Development of solid-state avalanche amorphous selenium for medical imaging. *Med. Phys.* **2015**, *42*, 1223–1226.
- (35) Kasap, S.; Frey, J. B.; Belev, G.; Tousignant, O.; Mani, H.; Laperriere, L.; Reznik, A.; Rowlands, J. A. Amorphous selenium and its alloys from early xeroradiography to high resolution X-ray image detectors and ultrasensitive imaging tubes. *Phys. Status Solidi B* **2009**, *246*, 1794–1805.
- (36) Reznik, A.; Baranovskii, S.; Rubel, O.; Jandieri, K.; Kasap, S.; Ohkawa, Y.; Kubota, M.; Tanioka, K.; Rowlands, J. Avalanche multiplication in amorphous selenium and its utilization in imaging. *J. Non. Cryst. Solids*. **2008**, *354*, 2691–2696.
- (37) Han, Z.; et al. High spatial resolution direct conversion amorphous selenium X-ray detectors with monolithically integrated CMOS readout. *Journal of Instrumentation* **2023**, *18*, P04021.
- (38) Rooks, M.; Abbaszadeh, S.; Asaadi, J.; Febbraro, M.; Gladen, R.; Gramellini, E.; Hellier, K.; Blaszczyk, F. M.; McDonald, A. Development of a novel, windowless, amorphous selenium based photodetector for use in liquid noble detectors. *Journal of Instrumentation* **2023**, *18*, P01029.
- (39) Mukherjee, A.; Vasileska, D.; Goldan, A. Hole transport in selenium semiconductors using density functional theory and bulk Monte Carlo. *J. Appl. Phys.* **2018**, *124*, 235102.
- (40) Mukherjee, A.; Akis, R.; Vasileska, D.; Goldan, A. Multiscale Modeling of High Field Hole Transport and Excess Noise in Avalanche Amorphous Selenium Layers. *2020 IEEE Nuclear Science Symposium (NSS) and Medical Imaging Conference (MIC)*; IEEE, 2020; pp 1–3.
- (41) Mukherjee, A.; Akis, R.; Vasileska, D.; Goldan, A. A Monte Carlo solution to hole transport processes in avalanche selenium semiconductors. *Physics and Simulation of Optoelectronic Devices XXVIII*; SPIE, 2020; p 112740U.
- (42) Mukherjee, A. A Study of Hole Transport in Crystalline Monoclinic Selenium Using Bulk Monte Carlo Techniques. M.Sc. thesis, Arizona State University, 2017.
- (43) Ridley, B. Lucky-drift mechanism for impact ionisation in semiconductors. *J. Solid State Phys.* **1983**, *16*, 3373.
- (44) Kasap, S.; Rowlands, J.; Baranovskii, S.; Tanioka, K. Lucky drift impact ionization in amorphous semiconductors. *J. Appl. Phys.* **2004**, *96*, 2037–2048.
- (45) Rubel, O.; Baranovskii, S.; Zvyagin, I.; Thomas, P.; Kasap, S. Lucky-drift model for avalanche multiplication in amorphous semiconductors. *Phys. Status Solidi C* **2004**, *1*, 1186–1193.
- (46) Jandieri, K.; Rubel, O.; Baranovskii, S.; Reznik, A.; Rowlands, J.; Kasap, S. Lucky-drift model for impact ionization in amorphous semiconductors. *J. Mater. Sci. Mater. Electron.* **2009**, *20*, 221–225.
- (47) Kabir, M.; Hijazi, N. Temperature and field dependent effective hole mobility and impact ionization at extremely high fields in amorphous selenium. *Appl. Phys. Lett.* **2014**, *104*, 192103.
- (48) Hijazi, N.; Kabir, M. Mechanisms of temperature-and field-dependent effective drift mobilities and impact ionization coefficients in amorphous selenium. *Can. J. Phys.* **2015**, *93*, 1407–1412.
- (49) Rubel, O.; Potvin, A.; Loughton, D. Generalized lucky-drift model for impact ionization in semiconductors with disorder. *J. Condens. Matter Phys.* **2011**, *23*, 055802.
- (50) Mukherjee, A.; Vasileska, D.; Akis, J.; Goldan, A. H. Monte carlo solution of high electric field hole transport processes in avalanche amorphous selenium. *ACS Omega* **2021**, *6*, 4574–4581.